J. Mech. Phys. Solids 157 (2021) 104605

Contents lists available at ScienceDirect

Journal of the Mechanics and Physics of Solids

journal homepage: www.elsevier.com/locate/jmps

Wave propagation in granular material: What is the role of particle shape?

X. Tang, J. Yang *

Department of Civil Engineering, The University of Hong Kong, Pokfulam Road, Hong Kong, China

ARTICLE INFO

Keywords:
Elastic wave propagation
Granular materials
Particle shape
Dispersion
Micromechanics

ABSTRACT

Wave propagation in granular materials is one of the most fundamental problems in mechanics and physics, with both scientific fascination and practical importance. Whether elastic waves in granular media are affected by particle morphology and, if yes, how they are affected remain open questions. Here we present a novel grain-scale model to address these fundamental questions. Efficient techniques are incorporated in the model to cope with a huge number of non-spherical particles which are randomly packed to propagate elastic waves. The variability of particle shape is mathematically described using the superquadric function and a family of geometric shapes is produced so that a systematic investigation of the effect of particle shape becomes viable. The difficulty with the detection of particle contacts that are represented by nonlinear Hertzian contact law is tackled using an efficient algorithm. A marked finding from the multiple series of simulations using this new model is that: an increase in the aspect ratio of particles (i.e. particles changing from spherical to ellipsoidal) leads to a notable rise in the elastic wave velocity, for both compression and shear waves, whereas for non-spherical particles with a given aspect ratio, an increased particle blockiness causes a moderate reduction in the wave velocity. Moreover, it is found that an assembly of particles with higher aspect ratio is associated with a broader range of transmitted frequencies while an assembly of particles with magnified blockiness holds back the conduction of higher frequencies. Based on statistical analyses, we further show that the transition from spherical to non-spherical particles is associated with a broader range of void ratios and increased coordination numbers whereas inflated blockiness brings an opposite impact, and these changes are linked with the observed effect of particle shape on the characteristics of elastic waves, in both time and frequency domains.

1. Introduction

Granular materials refer to a broad class of natural and synthetic materials which are composed of discrete particles interacting with each other when subjected to loading. These materials behave differently from usual solids, exhibiting many salient features such as fabric anisotropy, stress dilatancy, nonlinear elasticity and density dependence. The mechanical behavior of granular materials is a subject of long-standing interest in many fields, with both scientific fascination and practical importance (Spencer, 1964; Rudnicki and Rice, 1975; Walton, 1987; Satake and Jenkins, 1988; Nedderman, 1992; Jaeger et al., 1996; McDowell et al., 1996; Nixon and Chandler, 1999; Anand and Gu, 2000; Rothenburg and Kruyt, 2004; Yang and Wei, 2012; Andreotti et al., 2013; Goddard, 2014; Yang

* Corresponding author.
E-mail address: junyang@hku.hk (J. Yang).

https://doi.org/10.1016/j.jmps.2021.104605
Received 5 April 2021; Received in revised form 26 July 2021; Accepted 3 August 2021
Available online 15 August 2021

and Luo, 2015; Kawamoto et al., 2018; and the refenreces therein).

Among the variety of problems related to granular materials, wave propagation is a particularly interesting one yet remains poorly understood. The classic work of Duffy and Mindlin (1957) found that the sound velocity in a face-centered cubic packing of steel beads scales with the power of 1/4 of the confining pressure rather than the power of 1/6 predicted by the Hertz contact law. Considerable efforts have been made to seek explanations for the discrepancy: some researchers attributed it to the actual steel beads being not perfect elastic spheres (Goddard, 1990) whereas some others attributed it to the randomness of the contact lattice (Roux, 1997; Gilles and Coste, 2003) or, more fundamentally, to the change of fabric in response to the applied load (Gu and Yang, 2013).

Using piezoelectric transducers (also known as bender elements in the literature), Sharifipour et al. (2004) measured the shear wave velocity in confined assemblies of mono-sized glass beads and showed that the shear wave velocity increases with increasing size of glass beads. Interestingly, an opposite finding was reported by Patel et al. (2009), also for assemblies of glass beads, that the shear wave velocity decreases with increasing size of glass beads. Noting the contradictory results, Yang and Gu (2013) set up a sophisticated apparatus incorporating both bender element and resonant column techniques to measure shear waves in confined assemblies of uniformly graded glass beads. For a range of packing densities and confining pressures, they showed that the shear wave velocity is almost independent of the size of glass beads; they also proposed that the diverse views were probably caused by the uncertainties involved in wave signal interpretation. In a typical experimental setup for wave propagation in granular packings (Fig. 1), wave velocities are often deduced from the time-of-flight measurements of signals, which are usually masked by the complex near-field effects associated with scattering and diffusion (Yamashita et al., 2009; Gu et al., 2013).

Most of the experimental studies were conducted on assemblies of spherical particles (e.g. steel beads and glass beads). In real world problems, the constituent particles of granular materials are often not spherical but exhibit great variability in shape. There is a growing interest in the role of particle shape in the overall mechanical response of granular materials (De Graaf et al., 2011; Wei and Yang, 2014). Of recent notable studies, Yang and Luo (2015) established quantitative relationships between particle shape parameters, including sphericity, convexity, aspect ratio and overall regularity, and the critical state parameters through a specifically-designed experimental program in conjunction with the critical state theory. These relationships offer a promising pathway to the construction of macro-scale constitutive models with micro-scale properties built in. Some interesting experimental observations, such as why a granular material with rounded particles is more susceptible to triggering of instability than a granular material composed of angular particles, can be explained rationally using these relationships.

Compared with the quasi-static behavior, how elastic waves are affected by grain shape remains poorly understood. Cho et al. (2006) reported data for a range of natural and crushed sands showing that a decrease in roundness of sand grains leads to a decrease in shear wave velocity or shear stiffness. Liu and Yang (2018) re-examined the data and speculated that the observed changes in shear wave velocity were likely caused by the variations of particle size distribution (i.e. particle gradation) of the different sands tested, rather than by the variations of particle shape. To eliminate the influence of particle gradation, they specifically prepared four natural sands with *similar* particle gradations but *different* particle shapes in the laboratory, and measured shear waves in cylindrical specimens of these sands for a range of packing densities and confining pressures. The results indicate that under otherwise similar conditions, a sand specimen composed of angular grains has a higher shear wave velocity or shear stiffness than that composed of rotund particles. While the experiments and arguments of Liu and Yang (2018) appear to be sound, the divergent views underline the complexity of the problem and the need for further research. It is particularly desirable to elucidate the mechanisms underlying the various experimental observations.

The complexity of the problem originates primarily from the particulate nature of granular materials: that is, the overall mechanical response of a granular material is highly dependent on the packing pattern and interactions of the constituent particles which are, further, closely related to particle shape and gradation. In laboratory experiments, it is difficult, if not impossible, to accurately measure and quantify the packing pattern and contact conditions of a granular packing and their evolutions under external

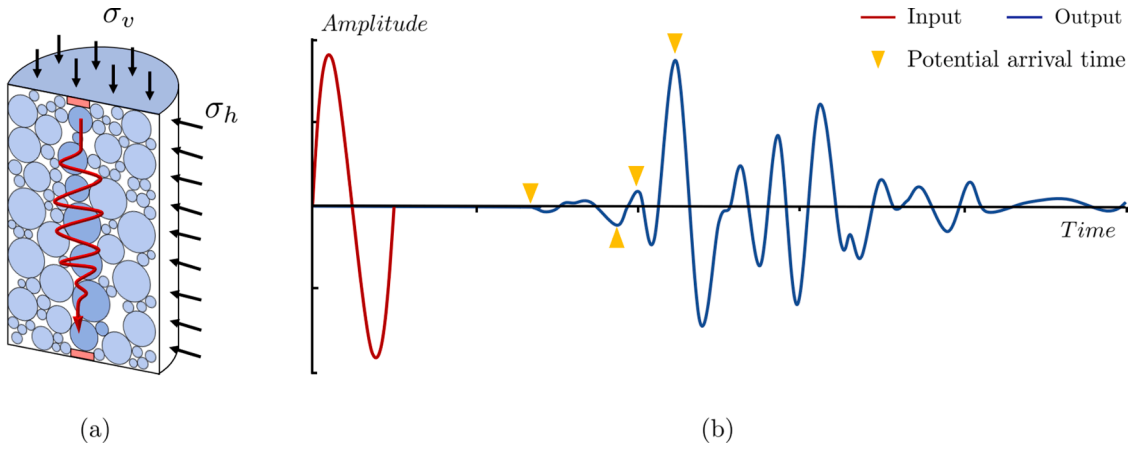

Fig. 1. (a) Illustration of typical experimental setup of wave propagation in granular materials; (b) Uncertainties in the determination of first arrival time in wave signal analysis due to near-field effect.

perturbations. The problem is further complicated by the phenomena of dispersion, attenuation, scattering and filtering associated with the wave propagation in granular media (Jia, 2004; Brunet et al., 2008; Vergara, 2010; Yang and Gu, 2013; Leonard et al., 2014; Waymel et al., 2018; Saitoh et al., 2019). To achieve a full understanding of the wave propagation in granular media, one needs to properly account for the granular nature.

In this paper, we present a novel grain-scale model for wave propagation in granular media with the aim to explore the role of particle morphology. The modeling technique is built upon the principles of the discrete element method (Cundall and Strack, 1979) by assuming that the individual particles in a granular assembly displace only through interactions with each other at contact points. While the discrete element method (DEM) has been increasingly used to model the quasi-static behavior of granular materials, few attempts were made to model the problem of wave propagation (Somfai et al., 2005; Mouraille and Luding, 2008; O'Donovan et al., 2015; Cheng et al., 2020), due probably to the significant difficulties and uncertainties involved. As a typical dynamic problem, the boundaries of any numerical model need to be properly treated since the reflections and refractions off the boundaries can intervene the wave signal. The model size is also a critical concern: if the size is small, the near-field effect may become pronounced leading to considerable uncertainties in identifying the first arrival of the elastic wave and, subsequently, the wave velocity and the dispersion relation. Difficulty also exists in simulating the transmitter and receiver in a numerical specimen as analogous to the bender elements in physical experiments, since the insertion of the elements may disturb the granular packing and affect the signals. When particle shape and gradation are concerned, extra challenges arise. As a result, available attempts have focused mainly on regular packings (e.g. face-centered cubic packing) and exclusively on 2D circular or 3D spherical particles.

In this study, we introduce efficient techniques to cope with a huge number of 3D non-spherical particles which are randomly packed to propagate elastic waves generated by very small perturbations. The variability of particle shape is mathematically described using the superquadric function and a family of geometric shapes is produced for systematic investigation of the effect of particle shape (Fig. 2). Compared with the clumped particles which are widely used in current DEM simulations of granular materials, the superquadric particles have some significant advantages. They overcome the drawback of clumped particles that the contact detection and contact force evaluation merely depend on the constituent spheres and associated radii – this drawback can result in abnormally high contact numbers and inaccurate rotational movements of the clumps in certain situations (Lu et al., 2015; Soltanbeigi et al., 2018). There is a big challenge, however, when using the superquadric particles, i.e. the curvature-related calculations in contact detection and the associated constraints of computation capacity. Probably due to this difficulty, there are only several attempts in the literature, made for packings with a small number of superquadric particles and with simplified contact laws and for the quasi-static behavior (Wellmann et al., 2008; Podlozhnyuk et al., 2017; Zhao et al., 2018).

The present study is the first attempt to implement superquadric particles for investigating the effect of particle shape on wave propagation in granular media. A huge number of superquadric particles, at the level of several hundreds of thousands, are randomly packed such that the packing dimensions are scaled up to that comparable with the physical experiment. An efficient algorithm is developed to detect particle contacts that are represented by nonlinear Hertzian contact law. The fundamental questions to be addressed here include: (a) what are the characteristics of elastic wave propagation, in both time and frequency domain, and how they are affected by particle shape; (b) what is the interplay of the effect of particle shape with the effects of packing density and confining pressure; and (c) what are the micromechanical mechanisms underlying the effects observed at the macroscale.

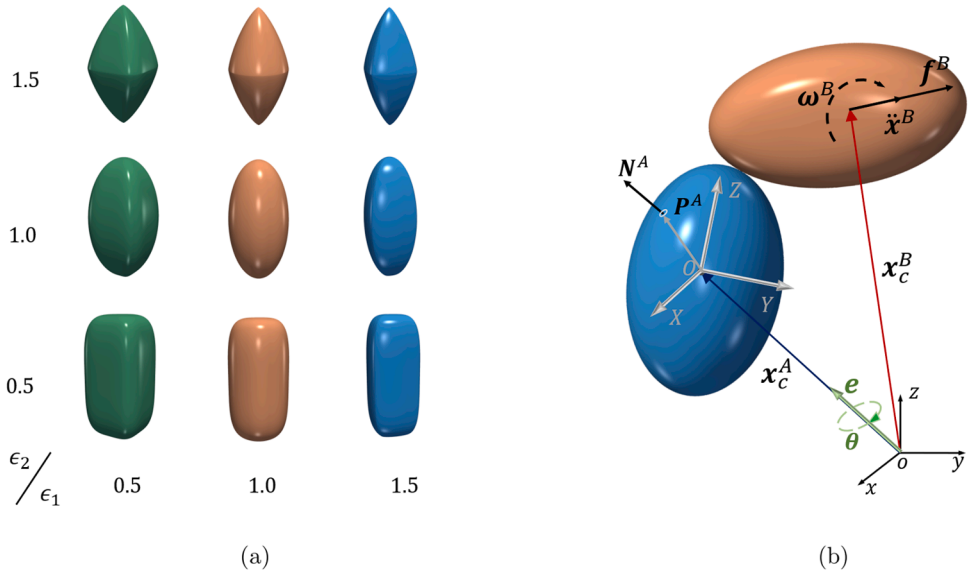

Fig. 2. (a) Illustration of basic properties of superquadric particles: (a) A cluster of irregular shapes manipulated by parameters ϵ_1 and ϵ_2; (b) Tracking particle position and orientation by position vector and rotational matrix between the local and global coordinate systems.

2. Superquadric particles and contact evaluation

2.1. Description of particle shape

As initiated in computational graphics, superquadrics have been extensively used to resemble a wide spectrum of natural shapes (Terzopoulos and Metaxas, 1991). The contours of superquadric particles are intuitively determined by five geometric parameters, and the surface function is usually expressed in a closed form as (Barr, 1981):

$$F(X,\ Y,\ Z) = \left(\left|\frac{X}{r_1}\right|^{\frac{2}{\epsilon_1}} + \left|\frac{Y}{r_2}\right|^{\frac{2}{\epsilon_1}} \right)^{\frac{\epsilon_1}{\epsilon_2}} + \left|\frac{Z}{r_3}\right|^{\frac{2}{\epsilon_2}} - 1 \tag{1}$$

where r_1, r_2 and r_3 are semi-axis lengths in the principal directions X, Y and Z, respectively; ϵ_1 and ϵ_2 are shape parameters that could be used to control the sharpness or roundness. As illustrated by a 3×3 grid in Fig. 2, the convex-shaped particle can be generated by varying ϵ_1 and ϵ_2, where the aspect ratios are consistently controlled as $r_3 = 2r_1 = 2r_2$. It is convenient to distinguish the relative position of a point based on Eq. (1): for a point inside the particle, we have $F < 0$, while a surface point is defined by $F = 0$. Otherwise, the points are located outside of the superquadric particle. In addition, the closed form of surface function facilitates the curvature and contact profile calculation for grain-scale simulations.

2.2. Description of particle motion

Unlike spherical particles, the superquadric particles do not possess isotropic inertia at all directions, and updating the rotational motion needs to be specially solved along with the extended integration scheme. In general, the translation and rotational motion of a particle can be expressed as:

$$\boldsymbol{f}^{(i)} = m^{\mathscr{P}^{(i)}} \ddot{\boldsymbol{x}}^{(i)} \tag{2}$$

$$\boldsymbol{t}^{(i)} = \boldsymbol{I}^{(i)} \cdot \boldsymbol{\omega}^{(i)} + \boldsymbol{\omega}^{(i)} \times \boldsymbol{I}^{(i)} \cdot \boldsymbol{\omega}^{(i)} \tag{3}$$

where super-script i denotes the label for particle $\mathscr{P}^{(i)}$ inside the domain, $\boldsymbol{f}^{(i)}$ and $\boldsymbol{t}^{(i)}$ are the resultant force and torque with regard to the center for $\mathscr{P}^{(i)}$, respectively; $m^{\mathscr{P}^{(i)}}$ refers to the particle mass; $\ddot{\boldsymbol{x}}^{(i)}$ is the acceleration; $\boldsymbol{I}^{(i)}$ is the moment of inertia and $\boldsymbol{\omega}^{(i)}$ is the angular velocity. As shown in Fig. 2b, it is customary practice to create the quaternion updating the orientation:

$$\boldsymbol{q} = (q_0, q_1, q_2, q_3)^T = \cos(\theta/2) + \boldsymbol{e}\sin(\theta/2) \tag{4}$$

where $\boldsymbol{e}$ is the unit axis and θ is the rotation angle in global coordinate system. The quaternion gives access to construction of rotation

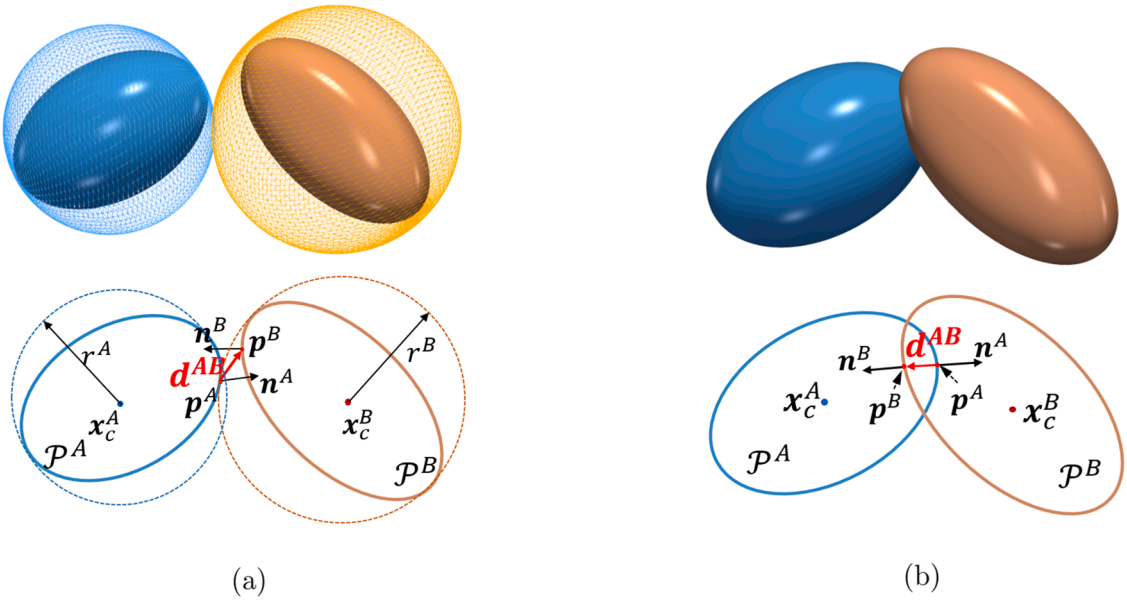

Fig. 3. Illustration of two-step contact detection program: (a) Direct exclusion of far-away pairs by bounding spheres; and quick exclusion of neighboring pairs by geometrical conditions; (b) Contact examination and determination of contact properties through the common normal concept.

matrix $\boldsymbol{R}$:

$$\boldsymbol{R} = \begin{bmatrix} 1-2\left(q_2^2+q_3^2\right) & 2(q_1q_2-q_0q_3) & 2(q_1q_3+q_0q_2) \\ 2(q_1q_2+q_0q_3) & 1-2\left(q_1^2+q_3^2\right) & 2(q_2q_3-q_0q_1) \\ 2(q_1q_3-q_0q_2) & 2(q_2q_3+q_0q_1) & 1-2\left(q_1^2+q_2^2\right) \end{bmatrix} \tag{5}$$

which makes the transformation between local and global quantities as conveniently as:

$$\boldsymbol{P} = \boldsymbol{R}^T \cdot (\boldsymbol{p} - \boldsymbol{x}_c) \tag{6}$$

$$\boldsymbol{N} = \boldsymbol{R}^T \cdot \boldsymbol{n} \tag{7}$$

where $\boldsymbol{R}^T$ is the transposed rotation matrix; $\boldsymbol{x}_c$ is the particle center in global coordinates; $\boldsymbol{p}$ and $\boldsymbol{P}$ are the point location in global and local coordinate systems, respectively; $\boldsymbol{N}$ and $\boldsymbol{n}$ are the unit outward normal at the surface point in local and global coordinate systems, respectively.

2.3. Contact detection

The difficulty with the use of superquadric particles is related to contact detection as the simple algorithm for spheres becomes invalid when it comes to non-spherical particles. Here, a two-step detection algorithm is introduced for irregular particle simulations (Fig. 3). First, a bounding sphere is created for each superquadric particle so that the potential contacts can be collected via a simple geometrical condition as below:

$$\| \boldsymbol{x}_c^A - \boldsymbol{x}_c^B \| \leq r^A + r^B + \delta_f \tag{8}$$

where $\boldsymbol{x}_c^A$ and $\boldsymbol{x}_c^B$ are the centers of two particles with contact potential; r^A and r^B are the radius of bounding sphere for objects A and B, respectively; δ_f is the distance factor that can be assigned as an absolute value or the ratio to the bounding radius. After the primary exclusion, the potential pairs of superquadric particles will be admitted to a shortlisted data structure, in which a more precise contact examination will be executed.

Then, the potential pairs are subjected to further detection by the common normal (CN) concept, which essentially specifies the geometrical conditions at actual contacts. This CN concept not only facilitates the check of non-touching neighbors, but also provides the quantities for contact force calculation (i.e. contact direction, penetration depth and contact profile). As specifically demonstrated in Fig. 3, contacts will eventually take place only if two conditions are fulfilled:

(i) the outward normals of two contacting objects, $\boldsymbol{n}^A$ and $\boldsymbol{n}^B$ are anti-parallel to each other:

$$\boldsymbol{n}^A + \boldsymbol{n}^B = \frac{\nabla f^A(\boldsymbol{p}^A)}{\| \nabla f^A(\boldsymbol{p}^A) \|} + \frac{\nabla f^B(\boldsymbol{p}^B)}{\| \nabla f^B(\boldsymbol{p}^B) \|} = \boldsymbol{0} \tag{9}$$

(ii) the penetration vector connecting two contact points, $\boldsymbol{d}^{AB} = \boldsymbol{p}^B - \boldsymbol{p}^A$, is parallel to the contact direction:

$$\left(\boldsymbol{p}^A - \boldsymbol{p}^B\right) \times \nabla f^B\left(\boldsymbol{p}^B\right) = \boldsymbol{0} \tag{10}$$

With reference to Eqs. (1) and (6), the shape function of a superquadric particle is noted as $f = f(x, y, z)$ in global coordinate system. Given the above basic formulations, the practical realizations may be achieved via various approaches, such as minimizing the difference between $\boldsymbol{d}^{AB}$ and $\boldsymbol{n}^B$ (or $\boldsymbol{n}^A$) (Lin and Ng, 1995; Kildashti et al., 2018). Concerning the generality and extendibility of the

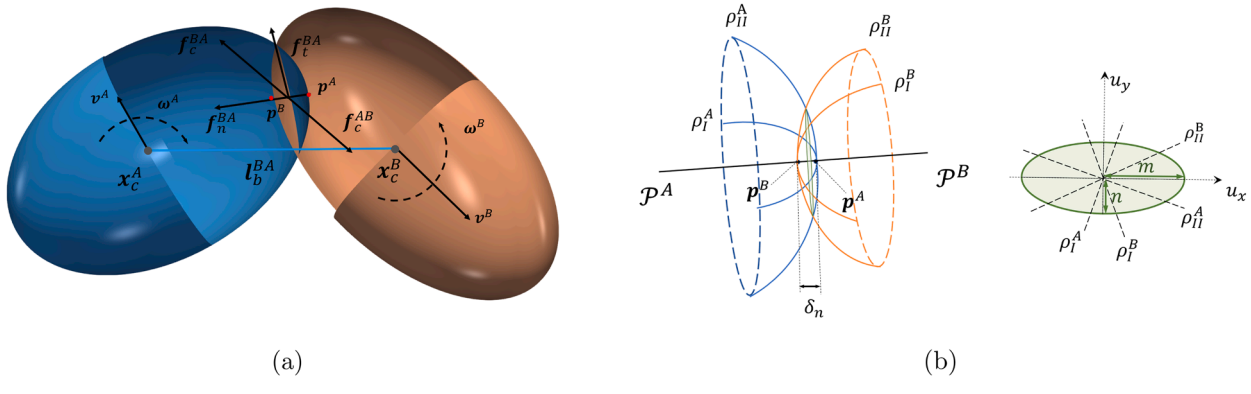

Fig. 4. Evaluating the contact force with Hertzian contact law for non-spherical smooth particles: (a) kinematics of contacting particles; (b) principal curvatures and contact profile at the contact.

algorithm, we preserve the set of non-linear equations in implicit surface forms. Along with $f^A(\boldsymbol{p}^A) = 0$ and $f^B(\boldsymbol{p}^B) = 0$, the equation set can be rearranged and solved by the modified Newton type optimization scheme (*i.e.* Line-Search method).

In the solving process, the iteration will be conditionally terminated as long as the potential pairs do not share real contacts, which can be checked against the condition below:

$$(\boldsymbol{p}^A - \boldsymbol{p}^B) \times \nabla f^B(\boldsymbol{p}^B) > \boldsymbol{0} \tag{11}$$

Similarly, if two objects are penetrating each other, it is natural to check the global position of two contact points if $\boldsymbol{p}^B \in \mathscr{P}^A$ as well as $\boldsymbol{p}^A \in \mathscr{P}^B$.

2.4. Implementation of Hertzian contact law

A vast majority of DEM simulations have practically simplified the computation in terms of particle shape (*e.g.* using spheres) and contact law (*e.g.* using the linear spring contact). As illustrated in Fig. 4, the overall contact force is denoted as $\boldsymbol{f}_c$ for simplicity so that $\boldsymbol{f}_c = \boldsymbol{f}_c^{BA} = -\boldsymbol{f}_c^{AB}$. Here, the nonlinear Hertzian contact law is adopted for the superquadric particles, for which the value of normal contact force, f_n, can be expressed as (Johnson, 1985):

$$f_n = K_n \delta_n = \frac{4}{3}\pi\eta\sqrt{\frac{\mathscr{S}(\xi)}{\mathscr{T}(\xi)^3(M+N)}}E^*\delta_n^{\frac{3}{2}} \tag{12}$$

with

$$M + N = \rho_I^A + \rho_{II}^A + \rho_I^B + \rho_{II}^B \tag{13}$$

$$\frac{1}{E^*} = \frac{(1-\nu^A)(1+\nu^A)}{E^A} + \frac{(1-\nu^B)(1+\nu^B)}{E^B} \tag{14}$$

in which K_n and δ_n are the normal-secant stiffness and normal contact overlap, respectively; E^* denotes the effective Young's modulus; $\eta = m/n$ is the *ratio* between semi-axes of contact profile with the assumption that $m > n$; $\mathscr{T}(\xi)$ and $\mathscr{S}(\xi)$ are the first kind and second kind elliptic integral with $\xi = \sqrt{1-(1/\eta)^2}$, respectively; M and N are relative curvatures; $\rho_I^{\blacksquare}$ and $\rho_{II}^{\blacksquare}$ are principal curvatures; $E^{\blacksquare}$ and $\nu^{\blacksquare}$ are the Young's modulus and Poisson's ratio for the object with $\blacksquare$ indicating contact body A or B, respectively (see Fig. 4).

Based on the Mindlin's no-slip solution (Mindlin, 1949), the tangential stiffness, $\boldsymbol{k}_t$, in both two principal directions of the contact profile should be considered:

$$\boldsymbol{k}_t = 2\pi m\left(H_1\mathscr{T}(\xi) - H_2\frac{\mathscr{T}(\xi)-\mathscr{S}(\xi)}{1-(m/n)^2}\right)^{-1}\boldsymbol{u}_x \otimes \boldsymbol{u}_x + 2\pi m\left(H_1\mathscr{T}(\xi) + H_2\frac{(m/n)^2\mathscr{T}(\xi)-\mathscr{S}(\xi)}{1-(m/n)^2}\right)^{-1}\boldsymbol{u}_y \otimes \boldsymbol{u}_y \tag{15}$$

with

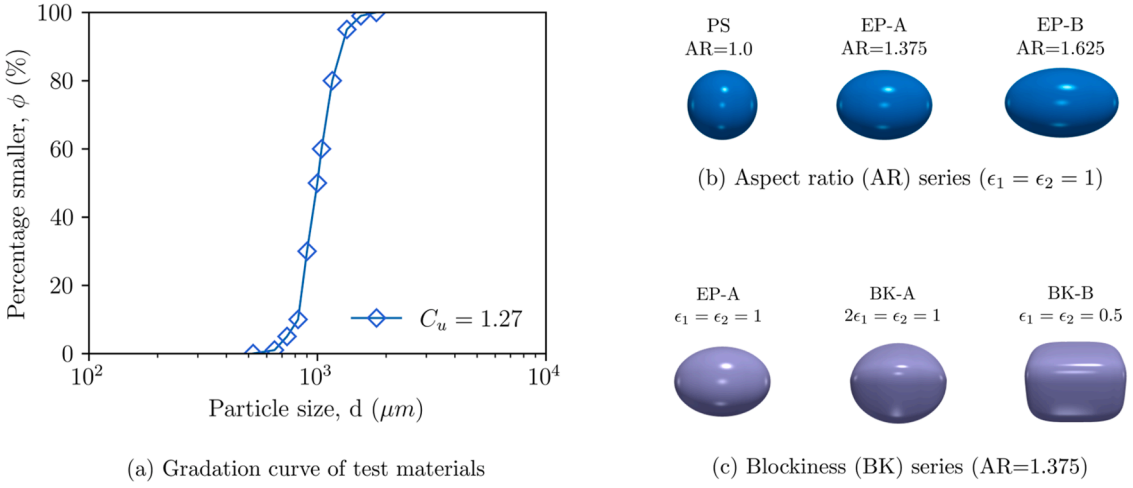

(a) Gradation curve of test materials

(b) Aspect ratio (AR) series ($\epsilon_1 = \epsilon_2 = 1$)

(c) Blockiness (BK) series (AR=1.375)

Fig. 5. Illustration of test materials: (a) Particle shape distribution (PSD) with $C_u = 1.27$; (b) Varying particle shape in terms of aspect ratio with $r_1 = r_2$; (c) Varying particle shapes in terms of blockiness with $r_1 = r_2$.

$$H_1 = \frac{1+\nu^A}{E^A} + \frac{1+\nu^B}{E^B} \qquad \text{and} \qquad H_2 = \nu^A \frac{1+\nu^A}{E^A} + \nu^B \frac{1+\nu^B}{E^B} \tag{16}$$

where $\boldsymbol{u}_x$ and $\boldsymbol{u}_y$ are the unit vector along the directions of semi-axes of the contact profile as illustrated in Fig. 4b. As the tangential force is always reloaded with contact history, the current tangential force, $\boldsymbol{f}_t^j$, is always calculated based on the value at previous step, $\boldsymbol{f}_t^{j-1}$:

$$\boldsymbol{f}_t^j = \boldsymbol{f}_t^{j-1} + \boldsymbol{k}_t \boldsymbol{v}^{AB} \Delta t \tag{17}$$

where $\boldsymbol{v}^{AB} = \boldsymbol{v}^B - \boldsymbol{v}^A$ denotes the relative velocity; j denotes the current count of timestep ($j \geq 1$); and Δt is the time step. In addition, the tangential force is always restrained by the Coulomb's friction law:

$$\boldsymbol{f}_t = \begin{cases} \boldsymbol{f}_t^j, & \text{if } \|\boldsymbol{f}_t^j\| \leq \mu |\boldsymbol{f}_n| \\ \mu |\boldsymbol{f}_n| \, \| \frac{\boldsymbol{f}_t^j}{\boldsymbol{f}_t^j} \|, & \text{else} \end{cases} \tag{18}$$

3. Numerical model of wave propagation

3.1. Test material and RVE generation

To eliminate the influence of particle gradation, a single particle size distribution (PSD), as shown in Fig. 5, is used in all numerical tests reported here. The particle size ranges from 2.0 mm to 0.5 mm, with the coefficient of uniformity $C_u = 1.27$ and the mean size $d_{50} = 1.0$ mm. The coefficient of uniformity is an index widely used in soil mechanics and is defined as the ratio of the sieve size through which 60% (by weight) of the particles passing to the sieve size that allows 10% of the particles to pass (i.e. $C_u = d_{60}/d_{10}$). Apparently, the coefficient is unity for mono-sized particles. Note that the size of a non-spherical particle is determined by its shortest semi-axis length following the principles of standard sieve tests in laboratory (Yang and Luo, 2015). The materials are categorized into two groups in terms of particle shape. The first group focuses on the aspect ratio of particles, by elongating the spheres to ellipsoids to give rise to three types of particles, namely PS, EP-A, EP-B (Fig. 5b). Here PS stands for purely spherical particle with the aspect ratio of 1, and EP-A and EP-B represent ellipsoids with the aspect ratio (r_3/r_1) of 1.375 and 1.625, respectively. The second group focuses on the blockiness of particles, by fixing the aspect ratio ($r_3/r_1 = 1.375$) and specifying different edge outlines (Fig. 5c): combination of $\epsilon_1 = 1$ and $\epsilon_2 = 0.5$ results in particles BK-A and combination of $\epsilon_1 = 0.5$ and $\epsilon_2 = 0.5$ gives rise to particles BK-B.

The strategy used in the grain-scale modeling here is to construct a representative volume element (RVE) as the basis for a larger, level-set specimen. The RVE is measured $20 \times 20 \times 20$ mm^3 and is bounded by period boundaries. Compared with the conventional boundaries such as rigid walls and membrane walls, the periodic boundary condition is useful in that the elastic wave propagation will not be terminated by edges and surfaces of the system. The average stress tensor is defined from the Love formula proposed by Christoffersen et al. (1981):

$$\boldsymbol{\sigma} = \frac{1}{V} \sum_{N_c} \boldsymbol{f}_c \otimes \boldsymbol{l}_b \tag{19}$$

where N_c refers to the total contact number, V is the cell volume, $\boldsymbol{l}_b$ is the branch vector joining two centers of particles, $\boldsymbol{f}_c$ is the contact force (Fig. 4).

The strain at each direction, ε_i, is simply calculated from the cell deformation:

$$\varepsilon_i = \frac{D_i(t) - D_i(t_0)}{D_i(t_0)} \tag{20}$$

where $D_i(t)$ and $D_i(t_0)$ are the periodic cell dimension at current and reference configurations ($i = 1, 2, 3$), respectively.

In constructing the level-set sample for wave propagation, superquadric particles are initially generated as non-contacting clouds in the periodic cell. It is to be noted that the number of particles in each cell depends on the corresponding shape parameter, since the cell size is fixed while the single particle volume varies. The initial orientations of non-spherical particles are *randomly* assigned and no preferable direction is allowed. The periodic cell is then subjected to isotropic consolidation through stress-controlled servo system as follows:

$$\dot{\boldsymbol{\varepsilon}} = \dot{\boldsymbol{\varepsilon}}_{\max} \frac{\boldsymbol{\sigma}_{tar} - \boldsymbol{\sigma}_{cur}}{\boldsymbol{\sigma}_{tar}} \tag{21}$$

where $\dot{\boldsymbol{\varepsilon}}_{max}$ is the input parameter that regulates the largest strain rate at one single step, $\boldsymbol{\sigma}_{tar}$ and $\boldsymbol{\sigma}_{cur}$ denote the target stress and current stresses. It can be seen that the convergence depends on the difference; the process is considered completed only when the stress tolerance and rattler fraction are stably below 0.001 % (*i.e.* one million timesteps). In order to assure the stability, the kinetic energy is artificially dissipated through local damping:

$$\boldsymbol{f}_{\mathrm{ad}} = -\gamma_{\mathrm{local}} \| \boldsymbol{f}^{\mathscr{P}} \| \mathrm{sign}\left(\boldsymbol{v}^{\mathscr{P}} \cdot \boldsymbol{f}^{\mathscr{P}}\right) \tag{22}$$

where $\boldsymbol{f}_{\mathrm{ad}}$ is the damping force that is fraction of particle resultant force; γ_{local} is the local damping coefficient, $\boldsymbol{f}^{\mathscr{P}}$, that acts in the opposite direction of particle velocity, $\boldsymbol{v}^{\mathscr{P}}$. The coordination number, Z, is also used to evaluate the practical completion of consolidation, which is defined as the ratio between contact entities and the number of particles:

$$Z = 2\frac{N_c}{N_p} \tag{23}$$

where N_c is the number of contacts, and N_p is the number of particles. As long as the consolidation is completed, local damping is turned *off*. As an example, Fig. 6 shows the periodic cells with varying particle shapes prepared at a similar state in terms of void ratio (~0.539) and confining pressure (100 kPa).

3.2. Numerical techniques for wave test

The intrinsic feature of periodic cell makes it possible to achieve the designed dimensions by replicating the prepared RVE in one or more directions. Here, the wave test specimen is made by gluing eleven RVEs in the direction of wave propagation (Cheng et al., 2020). After that, a calm-down process is conducted by introducing an artificial damping as:

$$\boldsymbol{f}_{\mathrm{vd}} = -\gamma_{\mathrm{vel}} \| \boldsymbol{v}^{\mathscr{P}} \| \mathrm{sign}\left(\boldsymbol{v}^{\mathscr{P}} \cdot \boldsymbol{f}^{\mathscr{P}}\right) \tag{24}$$

where $\boldsymbol{f}_{\mathrm{vd}}$ is the damping force caused by this damping mechanism, γ_{vel} is the velocity damping coefficient which usually falls into the range from 0.0 to 1.0, $\boldsymbol{v}^{\mathscr{P}}$ is the current velocity, and $\boldsymbol{f}^{\mathscr{P}}$ refers to the particle resultant force. The calm-down cycles are terminated once the average particle velocity is at or below 1.0×10^{-9} m/s. The calm-down process is crucial in that it guarantees all particles being practically quiet and hence the wave signal can be detected with possibly lowest agitation amplitude. To avoid reflections and refractions off the two end boundaries of the sample, we introduce a novel technique to freeze the two outer-most layers by fixing all degrees of freedom, as schematically shown in Fig. 7. The immediate neighboring layers are the cushion layers that can absorb kinetic energy based on Eq. (20). The thickness of each layer is equal to d_{50}.

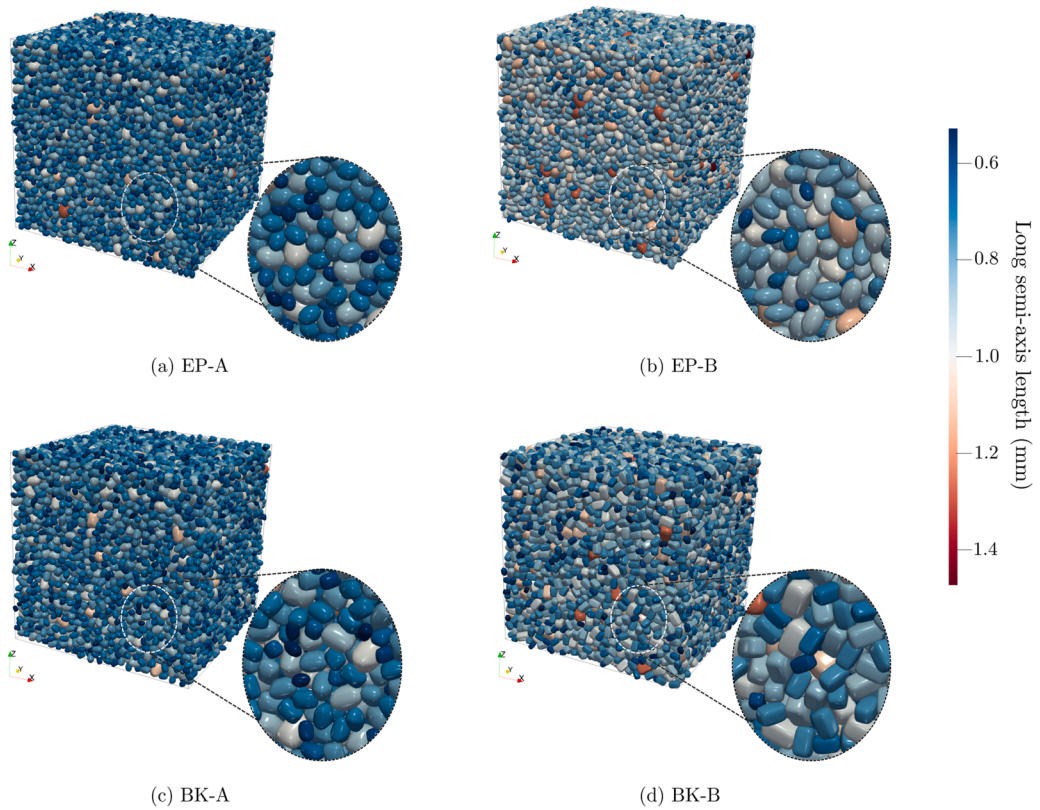

Fig. 6. Illustrations of prepared RVEs with different shape parameters (the colorbar refers to the range of long semi-axis length of superquadric particles).

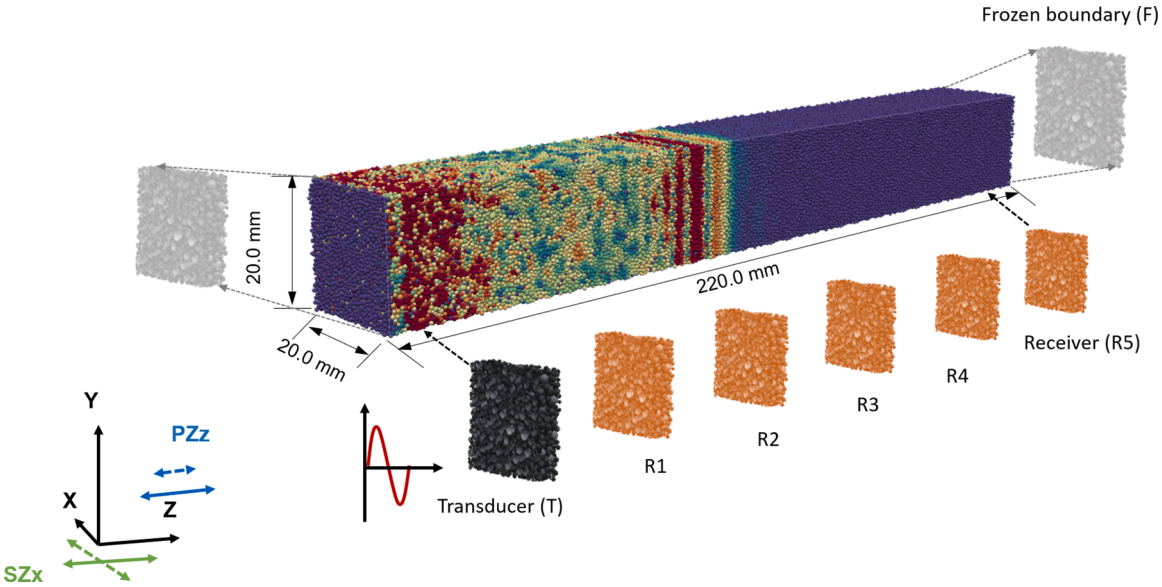

Fig. 7. Illustration of key elements involved in modelling wave propagation in enlarged granular medium. The input wave signal is agitated as single sine wave with minimum velocity amplitude and two types of elastic waves are considered.

The elastic wave is agitated close to one end of the specimen via a transmitter in the form of velocity at 1.0×10^{-3} m /s, which causes the maximum displacement below 1.0×10^{-8} m and preserves a very small strain regime. Then the wave will propagate towards the other end with minimal reflections and with the periodicity in other two directions. The input waveform is taken as single sine wave as in the laboratory test:

$$\boldsymbol{v}_{\text{in}} = \boldsymbol{A}_{\text{in}} \sin(\omega_{\text{in}} t) \tag{25}$$

where $\boldsymbol{A}_{\text{in}}$ is the amplitude of input signal in terms of velocity, $\omega_{\text{in}} = 2\pi f_{\text{in}}$ is the input angular frequency and f_{in} is the frequency. The input frequencies (f_{in}) are selected from 10 kHz to 400 kHz such that the an adequate range of wavelengths are covered and the near field effect can be avoided (Yang and Gu, 2013; Cheng et al., 2020). Both compression (P-) wave and shear (S-) wave tests are performed for each sample. The input parameters are summarized in Table 1. The material parameters in the table, including Young's modulus, Poison's ratio, coefficient of restitution and inter-particle coefficient, are typical for quartz grains. The two damping coefficients are used to efficiently prepare the specimen and assist the stability in consolidation of the specimen; they are turned *off* prior to the wave propagation test (i.e. the artificial damping is not activated in the wave test and hence does not influence the wave propagation). The input sine wave amplitude is set to be 10^{-3} m/s such that the strain level induced in the specimen is very small ($\sim 10^{-7}$ according to Bagi (1996)); this small-strain regime ensures the elastic wave propagation during which contact slip and fabric change barely happen.

Table 1
The key parameters used in the current DEM simulation of wave propagation

Terms	Value	Unit
Dimension of RVE	$0.02 \times 0.02 \times 0.02$	m^3
Dimension of long sample	$0.02 \times 0.02 \times 0.22$	m^3
Mean particle size, d_{50}	1.0	*mm*
Particle Young's modulus, E	70.0	GPa
Particle Poisson's ratio, ν	0.22	-
Particle restitution coefficient, C_r	0.95	-
Consolidation inter-particle friction, μ_{cons}	0.0 to 0.2475	-
Shear inter-particle friction, μ_{wave}	0.25	-
Input sine wave amplitude, A_{in}	1.0×10^{-3}	m/s
Input sine wave frequency, f_{in}	10 to 400	kHz
Time step, Δt	5.0×10^{-9}	s
Local damping coefficient, γ_{local}	0.1	-
Velocity damping coefficient, γ_{vel}	0.5	-

Table 2
Aspect ratio (AR) effect on elastic wave velocities.

Shape	Void ratio, e	Coord. number, Z	V_p (m/s)	V_s (m/s)
PS	0.549	5.901	540.23	355.50
EP-A	0.550	6.674	1367.33	915.32
EP-B	0.550	6.915	1374.43	932.44

3.3. Determination of wave velocity

In physical experiment, determining the wave velocity usually confronts many uncertainties and a unified method is almost impossible (Yamashita et al., 2009; Yang and Gu, 2013). To tackle this issue, we use multiple receivers placed along the propagation direction (abbreviated as R1 to R5 in Fig. 7). Accordingly, the peak-to-peak method is selected to determine the propagation speed at each receiver, and the time-of-flight velocity is the averaged value from all locations at a given input frequency. As a matter of fact, numerical experiment provide an easy access to monitoring and recording each particle and contact information at any time step and the dispersion relation can be generated by 2D Fourier transformation (Mouraille and Luding, 2008; Saitoh et al., 2019).

For any particle, $\mathscr{P}^{(i)}$, inside the long sample, its position is expressed as $\boldsymbol{x}^{(i)}$ and its velocity evolution with time $\boldsymbol{v}^{(i)}(t)$. With the wave vector $\boldsymbol{k}$, the Fourier transformation can be operated from time domain to wavenumber domain via position vector, which is expressed as:

$$\boldsymbol{v}_k(t) = \sum_{i=1}^{N} \boldsymbol{v}^{(i)}(t) e^{-I\boldsymbol{k}\cdot\boldsymbol{x}^{(i)}(t)} \tag{26}$$

which can generate the power spectrum of the particle velocity $\chi = |\boldsymbol{v}_k(\omega)|^2$ through Fourier transforms of $\boldsymbol{v}_k(t)$. The peak branch will be identified and fitted with the Lorentzian function, which can be expressed as:

$$\chi(k,\omega) = \frac{\chi_0 q(k)^2}{(\omega - \omega(k))^2 + q(k)^2} \tag{27}$$

where χ_0 denotes the peak value for the dominant angular frequency $\omega(k)$, and the physical meaning of $q(k)$ can be considered as the factor due to attenuation (Santamarina et al., 2001). The long-wavelength velocity is readily determined via the slope of peak branch with $\lim_{k\to 0}\omega(k)/k$.

Generally, the time-of-flight velocity has been widely adopted in physical tests, whilst the long-wavelength velocity commonly appears in theoretical investigations. Now there are two methods available to determine the elastic wave velocities. We use one specimen of perfect spheres (PS) to demonstrate how the S-wave velocities are determined by time-domain signals. This specimen is prepared with void ratio 0.540 at the isotropic confining pressure of 100 kPa. As demonstrated in Fig. 8, the wave velocities are approximately the same (i.e. ~358 m/s) extracted from receivers R1 to R4 with the input frequency 100 kHz. The time-of-flight velocity is found consistent with the wave velocity determined from dispersion relation. Based on the results validation, the averaged velocity from time domain will be used in the following wave velocities analysis, and the dispersion relation will be mainly used to characterize the propagation behaviors.

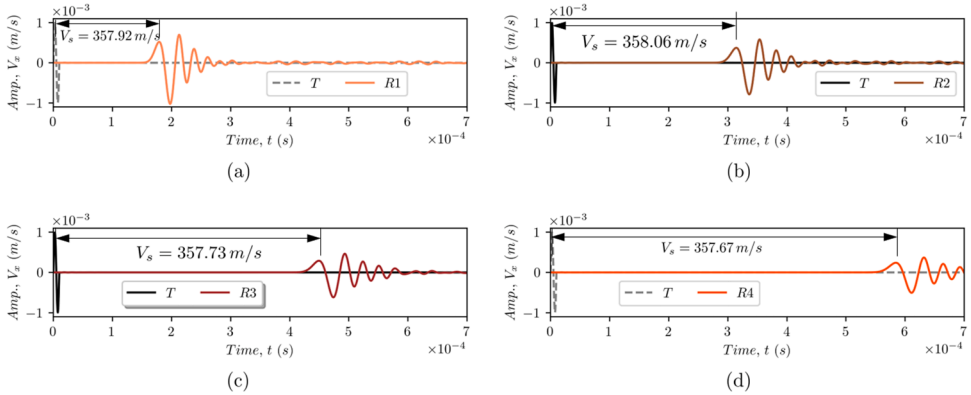

Fig. 8. Illustration of S-wave propagation in time domain and the determination of the S-wave velocity for PS specimen ($e = 0.540$, $\sigma_c = 100$kPa): The peak-to-peak method is used to calculate the distance-over-time velocity at each location and the final quantity is averaged among the consistent results at multiple receiver so that the uncertainties are avoided.

4. Results analysis

4.1. Analysis on wave propagation

Using the techniques described above, we have generated three numerical samples comprised of non-spherical particles with different aspect ratios but with almost identical void ratio under the isotropic confining pressure of 100 kPa. For clarity, these samples are named according to their shape, void ratio and stress state, abbreviated as PS-e-0.549-ISO100, EP-A-e-0.550-ISO100 and EP-B-e-0.550-ISO100, respectively. An exactly same agitation of small amplitude is applied in compression to each of the three samples, and the signals received at R3 are compared in Fig. 9. It is evident from Fig. 9 that for either compressional or shear agitation, elastic waves propagate at much higher speeds in EP-A and EP-B specimens compared to PS specimen, indicating a marked effect due to non-sphericity of particles (Table 2). Moreover, the waveforms in PS specimen exhibit different characteristics compared with the waveforms in EP-A and EP-B specimens, implying that the variation of particle shape alters the attenuation and dispersion of the waves.

To better evaluate the effect, further analysis of the dispersion relation is performed using 2D Fourier transformation, and the representative results are shown in Fig. 10. A cut-off frequency can be observed clearly in PS specimen: it is around 55 kHz for both compression wave and shear wave. When waves propagate in EP-A and EP-B specimens, the cut-off frequency increases to around 115 kHz, meaning that packings with non-spherical particles can propagate waves with higher frequencies. The sharp increase in the propagation velocity of both P and S waves and the dramatic rise of the cut-off frequency when particle shape is turned from spherical to ellipsoidal indicate the limitations of using assemblies of spherical particles to simulate the dynamic problems in reality. On the other hand, the difference introduced in the aspect ratio for ellipsoidal particles is found to produce a minor effect. The dispersion relation is useful for capturing the wave velocity as well as frequency spectrum at varying wavelengths, which relies on the careful treatment in the calm-down process as well as the boundary conditions. The wave attenuation can also be estimated using the Lorentzian function (Eq. (27)). For the dispersion data in Fig. 10, we quantify the attenuation coefficient as a function of wavenumber or frequency and observe that the Rayleigh law of scattering generally holds for both spherical and non-spherical particle packings (Fig. 11a and b). For either compression or shear wave, the attenuation in a packing of non-spherical particles is generally smaller than in a packing of spherical particles.

With the numerical setup and using EP-A (AR=1.375) particle as a reference, the particle outline has been further altered to investigate the impact of particle blockiness. Likewise, three specimens are created with similar void ratio of 0.500 under the same confining pressure of 100 kPa. The input signal and the received signal in each sample are shown in Fig. 12, for P wave and S wave, respectively. It is clear that the received waveforms are differing in both amplitude and frequency. The determined time-of-flight velocities are listed in Table 3, which shows that the velocity slightly decreases as the blockiness outline becomes cuboidal. For instance, the P-wave velocity drops from 1438.62 m/s to 1357.43 m/s as particle shape evolves from EP-A to BK-B. Fig. 13 compares the dispersion relations of P and S waves in the three specimens. In general, there is no notable difference except that the intensity of

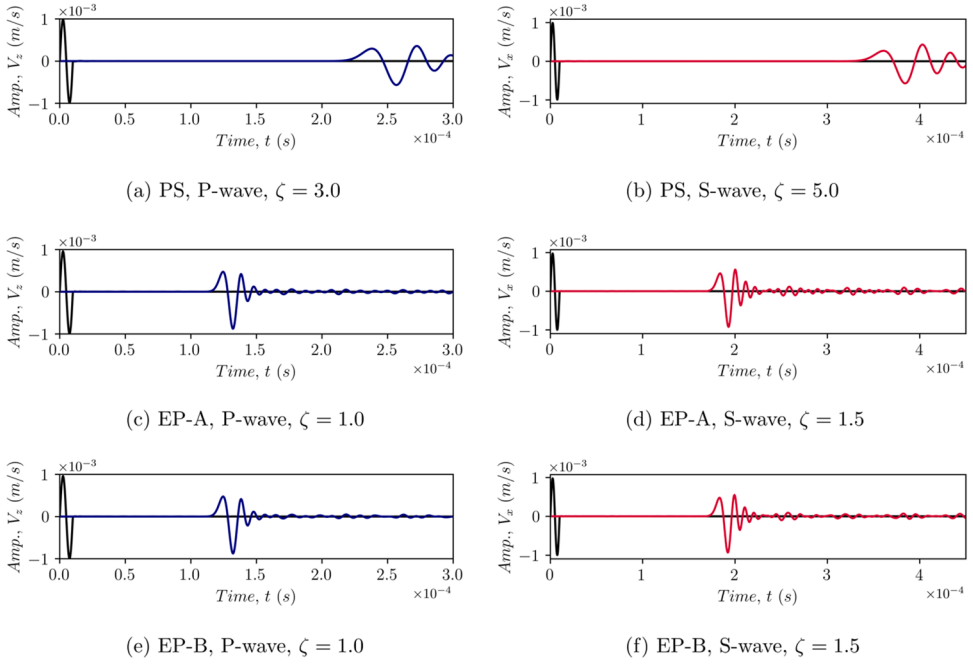

(a) PS, P-wave, $\zeta = 3.0$ (b) PS, S-wave, $\zeta = 5.0$

(c) EP-A, P-wave, $\zeta = 1.0$ (d) EP-A, S-wave, $\zeta = 1.5$

(e) EP-B, P-wave, $\zeta = 1.0$ (f) EP-B, S-wave, $\zeta = 1.5$

Fig. 9. Received wave signals at location R3 for aspect ratio test series with void ratio around 0.550 at the confining pressure of 100kPa: (a) (c) (e) P-wave; (b)(d)(f) S-wave. ζ denotes the amplification factor that magnifies the amplitude of output signals.

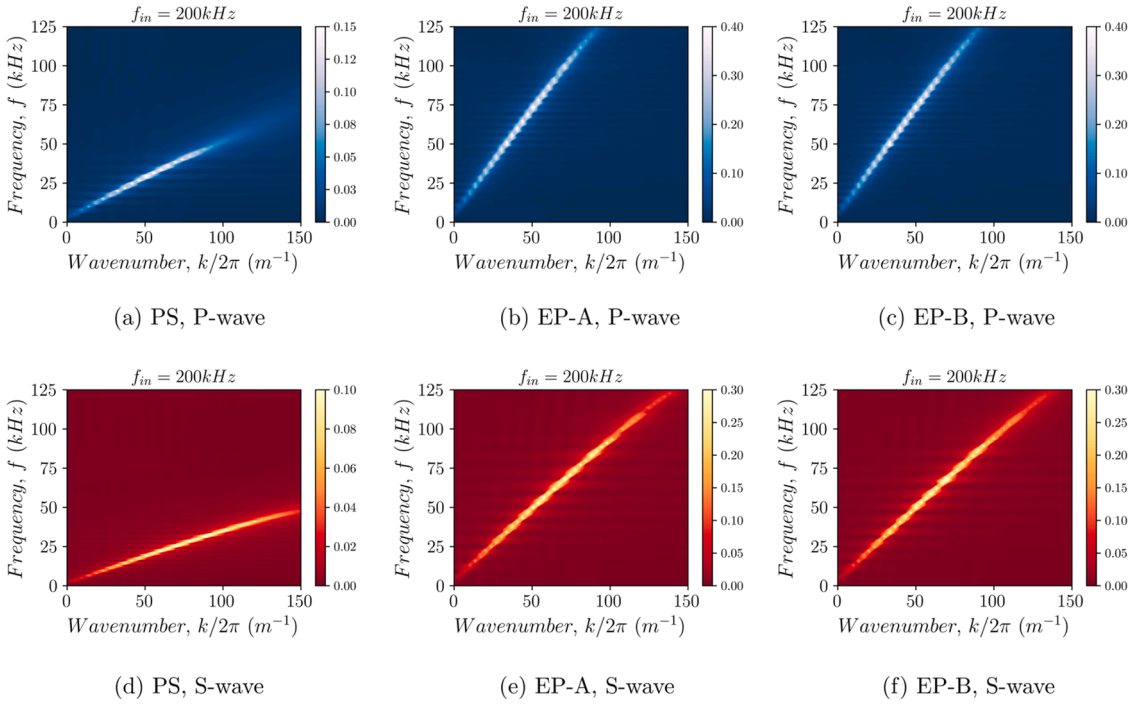

Fig. 10. Dispersion relations for aspect ratio test series specimens with void ratio around 0.550 at the confining pressure of 100kPa: (a) (b) (c) P-wave; (d) (e) (f) S-wave.

the peak branch for BK-B is lowered than that for EP-A. The observed noise in case BK-A potentially comes from the accidental disturbance to the contact located at edges, which becomes apparent periodically. Again, the long-wavelength velocity gives the consistent result that an increased blockiness reduces the propagation velocity of both P and S waves. As far as wave attenuation is concerned, it tends to increase as the blockiness of particle shape develops (Fig. 11c and d).

4.2. *Characterization of wave velocities*

We have shown solid evidence that the characteristics of elastic waves in a granular packing can be altered significantly when the particle shape changes from spherical to ellipsoidal. Since the elastic wave velocity in a granular material is highly dependent on the packing density (void ratio) and confining pressure, it is of great interest to further explore the interplay of the particle shape and the initial state. In doing so, a large number of numerical specimens are prepared for AR test series, which cover a broad range of packing states in terms of void ratio and confining pressure. At each state, both P-wave and S-wave tests are performed, and the results on wave velocities are plotted in Fig. 14. At first glance, packings of ellipsoidal particles (EP-A and EP-B) tend to achieve denser states and exhibit a wider range of void ratio compared to spherical packings (PS), despite that they have the same particle size distribution. For all pressure levels considered, the elastic wave velocities are markedly higher in EP-A and EP-B specimens than in PS specimens. These results lend support to the findings of the recent laboratory tests of Liu and Yang (2018), who showed that the specimens of sub-angular Fujian sand exhibit higher shear wave velocity than the specimens of sub-rounded Ottawa sand. Furthermore, Fig. 14 shows that at a given confining pressure, the variation range of wave velocity is more prominent for EP-A and EP-B specimens – this is due partly to the broader range of void ratio. It is also noticed that P-wave seems to be more sensitive to the confining pressure than S-wave.

To characterize the state dependence of wave velocity, we use the simple relations proposed by Hardin and Richart (1963) based on laboratory tests on sands:

$$V_p = \alpha_p (a_p - e)\sigma_c^{\beta_p} \tag{28}$$

$$V_s = \alpha_s (a_s - e)\sigma_c^{\beta_s} \tag{29}$$

where the sub-scripts p and s denote P-wave and S-wave, respectively; a_*, α_* and β_* are fitting parameters for the two types of waves (with $* = p$ or s). Generally, either a_p or a_s will decrease as the confining pressure increases. The fitting parameters for wave velocities are summarized in Table 4, where a_p and a_s values are the averages for all confining stresses. It can be seen that as the particle shape turns from spherical to ellipsoidal, a_p decreases from 1.456 to 1.285 (EP-A) and 1.317 (EP-B). In contrast, a_s increases from 1.134 for PS to 1.162 for EP-A and 1.215 for EP-B. The variation of a_s is relatively small compared with a_p. As far as the stress exponent is concerned, it is reduced from 0.179 to around 0.070 for S-wave when particle shape changes from spherical to ellipsoidal. The implication is that

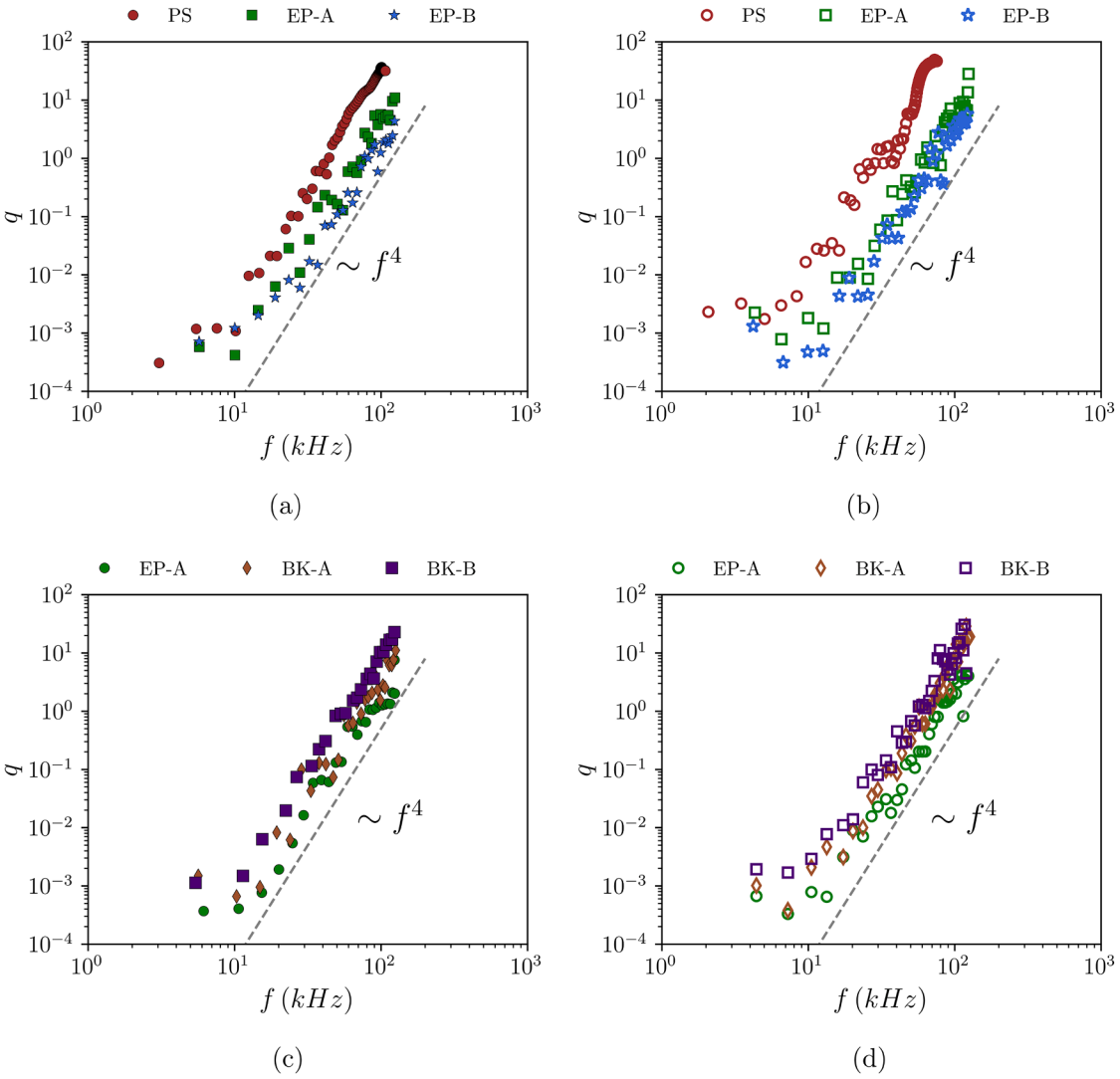

Fig. 11. Effect of shape parameters on wave attenuation coefficient q against dominant frequency f for each wavenumber k from the dispersion relation: (a) Aspect ratio P-wave test series; (b) Aspect ratio S-wave test series; (c) Blockiness P-wave test series; (d) Blockiness S-wave test series.

the elastic wave velocity has lower sensitivity to confining stress but higher correlation to void ratio for packings of elliptical particles. Note that the densest packing has a void ratio of 0.370 at the confining pressure of 100 kPa, which has the S-wave velocity of 1128.52 m/s. The loosest packing, by comparison, achieves a void ratio of 0.522 at the confining pressure of 1000 kPa, for which the shear wave velocity is 1113.27 m/s. With a wide range of void ratio, the fitting function results in larger value of α and lower value of β. To facilitate the direct comparison, the elastic wave velocities are normalized by the void ratio function and then plotted as a function of confining pressure, as shown in Fig. 15.

4.3. *Micromechanical perspectives*

Now, we make an attempt to seek the physical origins of the particle shape effect from the viewpoint of micromechanics. The effective medium theory (EMT) has been widely used in predicting the elastic modulus of granular packings with mono-sized spheres (Walton, 1987; Chang et al., 1995), which essentially links the macroscopic elastic properties and microscopic parameters. The P-wave and S-wave are directly related to the modulus via:

$$V_p = \sqrt{M_0/\rho_{\mathrm{d}}} \qquad \text{and} \qquad V_s = \sqrt{G_0/\rho_{\mathrm{d}}} \tag{30}$$

where M_0 and G_0 are the constrained modulus and shear modulus at small strain, respectively, and ρ_{d} is the dry sample density. Based on the EMT theory, given the isotropic confining stress σ_c, the general relationship has been established between wave velocities and

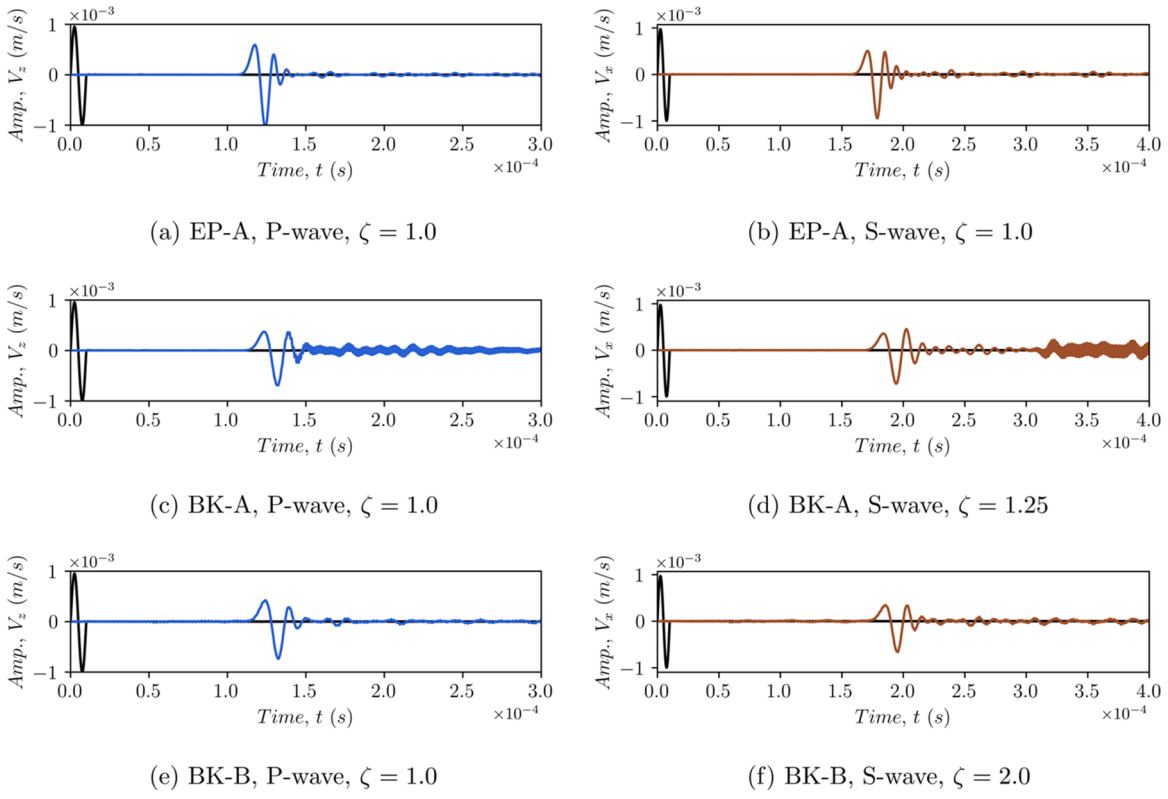

Fig. 12. Received wave signals at location R3 for blockiness test series with void ratio around 0.500 at the confining pressure of 100kPa: (a) (c) (e) P-wave; (b)(d)(f) S-wave. ζ denotes the amplification factor that magnifies the amplitude of output signals.

Table 3
Blockiness (BK) effect on elastic wave velocities.

Shape	Void ratio, e	Coord. number, Z	V_p (m/s)	V_s (m/s)
EP-A	0.501	7.364	1438.62	978.39
BK-A	0.500	6.457	1381.71	922.36
BK-B	0.499	6.429	1357.43	906.11

microscopic parameters yields (Jia et al., 1999):

$$V_* \sim Z^{1/3} e^{-1/3} \sigma_c^{1/6} \tag{31}$$

where V_* refers to the elastic wave velocity with sub-notation * as p or s; Z is the coordination number; e is the void ratio. In this study, the assemblies consist of randomly oriented grains with different shapes subjected to isotropic compression, and the wave agitation poses negligible impact on the packing pattern. Besides the coordination number, the representative parameters at the microscopic level also include fabric anisotropy and contact force distribution. The fabric tensor can be expressed as (Satake, 1976):

$$\boldsymbol{\Phi}_c = \int_{\Theta} E(\Theta) \boldsymbol{n}_c \otimes \boldsymbol{n}_c d(\Theta) = \frac{1}{N_c} \sum_{N_c} \boldsymbol{n}_c \otimes \boldsymbol{n}_c \tag{32}$$

where $\boldsymbol{n}_c$ is the contact normal, and Θ refers to the spatial orientation of $\boldsymbol{n}_c$ and $E(\Theta)$ refers to the spatial probability distribution function. As demonstrated by Oda (1982), it is sufficient to use the second order Fourier series approximating the fabric anisotropy:

$$E(\Theta) = \frac{1}{4\pi}[1 + \boldsymbol{a}_c : (\boldsymbol{n}_c \otimes \boldsymbol{n}_c)] \tag{33}$$

where $\boldsymbol{a}_c$ is always a deviatoric and symmetric second order tensor that is correlated to the fabric tensor above:

$$\boldsymbol{a}_c = \frac{15}{2} \mathrm{dev} \boldsymbol{\Phi}_c \tag{34}$$

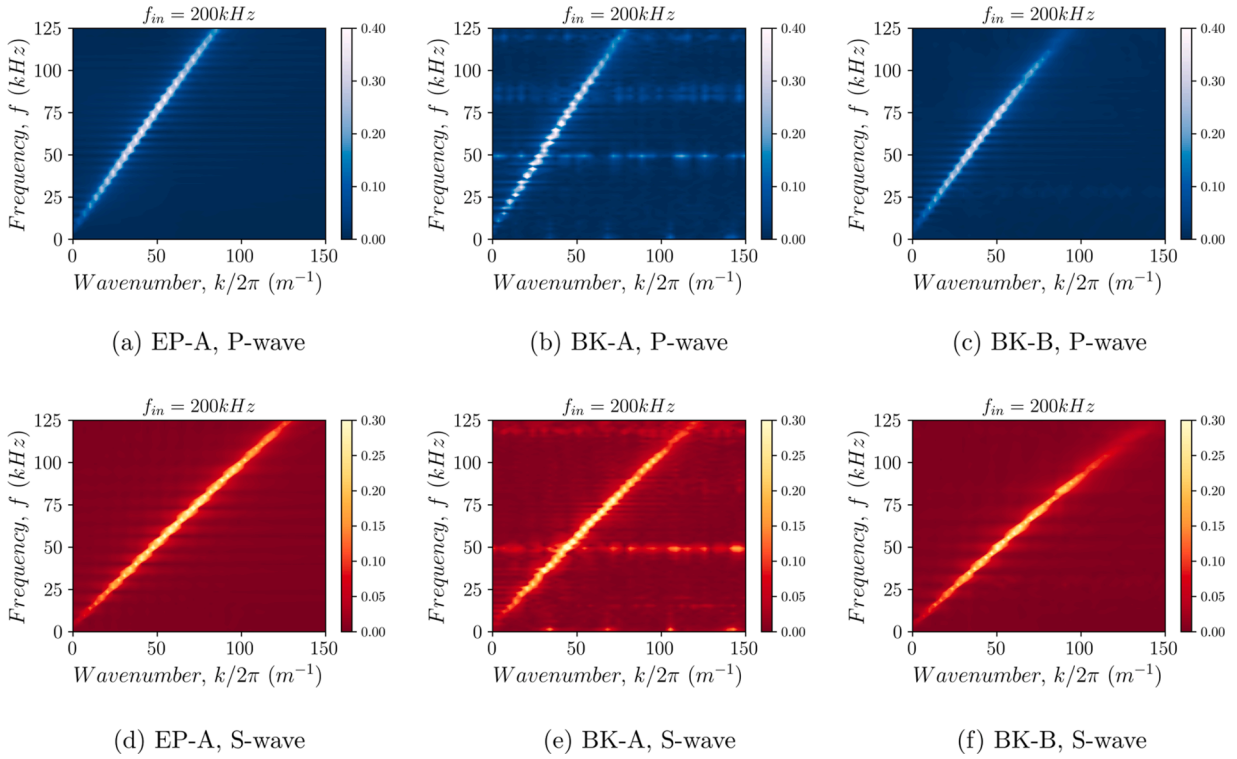

Fig. 13. Dispersion relations for blockiness test series specimens with void ratio around 0.500 at the confining pressure of 100kPa: (a) (b) (c) P-wave; (d) (e) (f) S-wave.

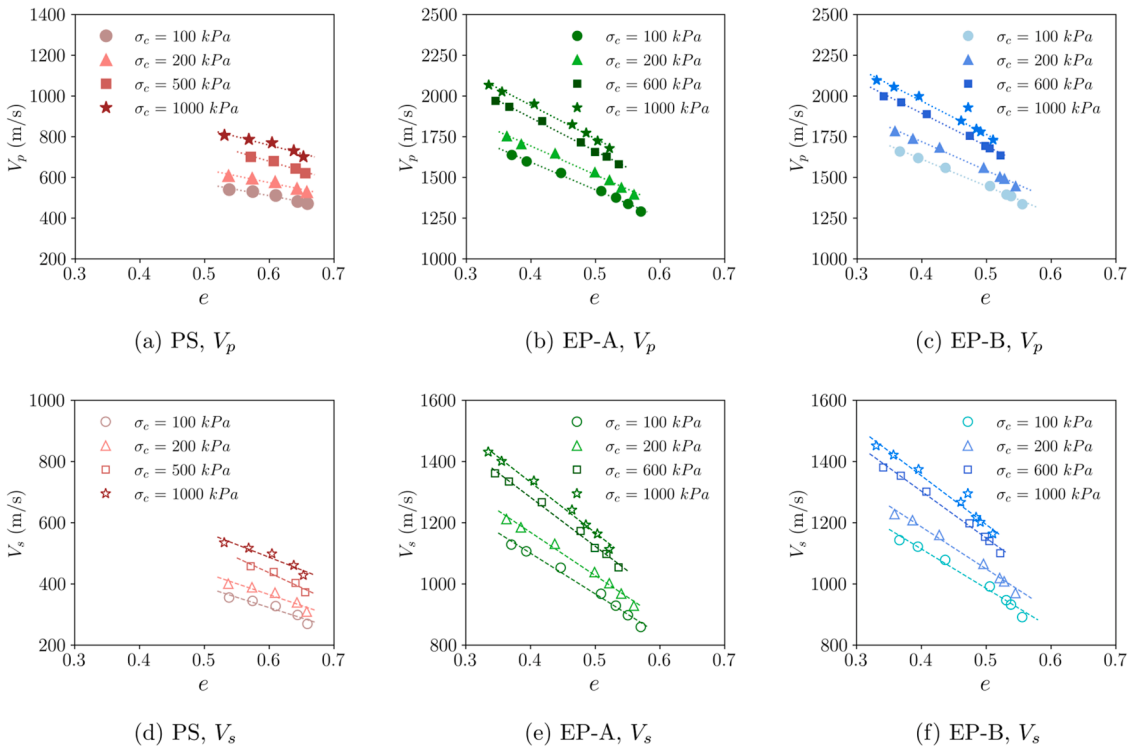

Fig. 14. Variation of elastic wave velocities under different isotropic confining pressures with different aspect ratios: (a) (b) (c) compression wave velocities V_p; (d) (e) (f) shear wave velocities V_s.

Table 4
Fitting parameters of elastic wave velocities with varying aspect ratios.

Shape	α_p	α_p	β_p	α_s	α_s	β_s
PS	1.456	267.337	0.173	1.134	263.469	0.179
EP-A	1.285	1319.616	0.072	1.162	1109.339	0.064
EP-B	1.317	1261.915	0.076	1.215	1015.501	0.070

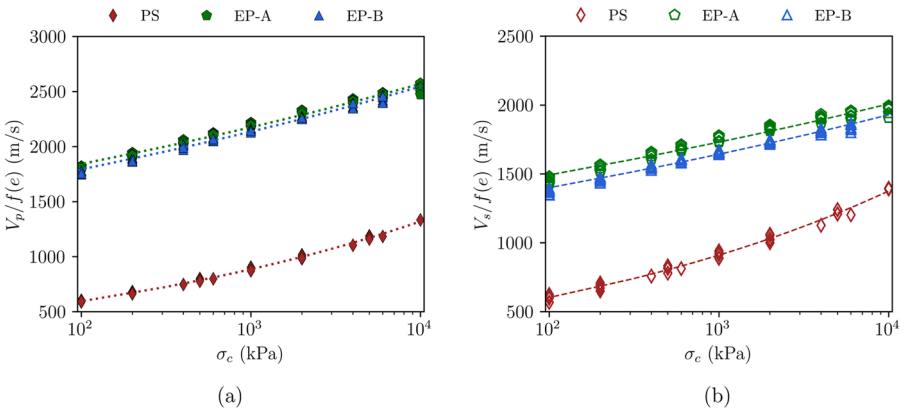

Fig. 15. Relationship between normalized elastic wave velocity and confining stresses with varying aspect ratio: (a) $V_p/f(e)$ vs σ_c; (b) $V_s/f(e)$ vs σ_c.

The degree of fabric anisotropy can then be quantified as:

$$a_c = \text{sign}(Q_a)\sqrt{\frac{3}{2}\boldsymbol{a}_c : \boldsymbol{a}_c} \quad \text{with} \quad Q_a = \frac{\boldsymbol{a}_c : \text{dev}\boldsymbol{a}_c}{\sqrt{\boldsymbol{a}_c : \boldsymbol{a}_c}\sqrt{\text{dev}\boldsymbol{a}_c : \text{dev}\boldsymbol{a}_c}} \tag{35}$$

For all RVEs prepared for this study, we estimate the degrees of fabric anisotropy and notice that the indicator a_c is always below 0.02. This implies that these RVEs possess an essentially isotropic fabric. In comparison, the fabric anisotropy usually refers to a much higher value (*e.g.* 0.60). Fig. 16 shows the coordination number as a function of void ratio for granular packings of different shapes. Besides the conventional coordination number in Eq. (23), the mechanical coordination number is proposed so that the rattlers with equal or less than one contact are eliminated (Thornton, 2000), which can be expressed as

$$Z_M = \frac{2N_c - N_p^1}{N_p - \left(N_p^0 + N_p^1\right)} \tag{36}$$

where N_p^0 denotes the number of particles without any contact, and N_p^1 refers to the number of particles with only one contact. And Z_M is deemed as a more precise indicator in quantifying the elastic properties of granular materials (Gu and Yang, 2013; Tang and Yang,

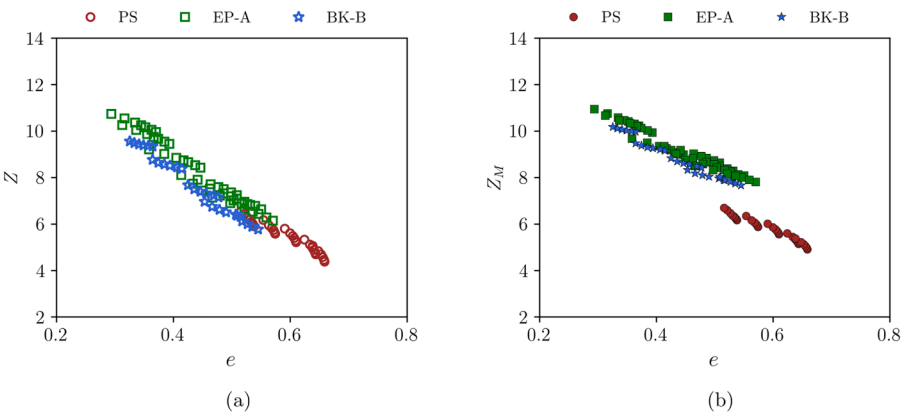

Fig. 16. Effect of particle shape on average contact number at the confining pressure from 50 kPa to 5000 kPa: (a) conventional coordination number against void ratio (Z vs e); (b) mechanical coordination number against void ratio (Z_M vs e).

2018). As shown in Fig. 16, the elongated particle packings cover a wider range of void ratio and obviously higher coordination numbers than the spherical particle packings. However, the increased blockiness leads to a slight shrink of upper bound void ratio and a reduction of coordination number. This observation is consistent with the previous study on random packing problems (Yuan et al., 2018). The observed variation in elastic wave propagation is well matched with the average contact number: the substantial change occurs when the spheres are elongated as ellipsoids, while further alteration towards quasi-cuboids will actually hold back such trend compared with pure ellipsoids. Aside from this observation, we also notice that the mechanical coordination number for non-spherical particles are apparently higher than the spherical particles, which partially explains why the conventional coordination number is barely able to elucidate the apparent shape effect on elastic wave velocities.

Since the contact of non-spherical particles are curvature related, the contact network of a granular packing is expected to be affected by the particle shape. As the particle shape varies, the distribution of contact normal stiffness evolves so that the different quasi-static regimes can be achieved at different confining pressures. Thus, it is interesting to quantify the homogeneity of specimens with varying shapes and the potential contributions to the mechanical properties. To make the point clear, three numerical samples with different particle shapes are prepared such that they have the same void ratio 0.552 and the same confining pressure of 50 kPa. The probability distributions of contact normal stiffness, K_N, are derived from the statistical analysis and are shown in Fig. 17. It is interesting to note that the general form of distribution is similar for PS and EP-A, whereas BK-B exhibits a notable difference. The distribution is obviously broader for BK-B. To quantify the distribution, we use Gaussian distribution and Weibull distribution functions as follows:

$$g(K_n,\mu,\sigma)=\frac{1}{\sqrt{2\pi}\sigma}\exp\left(-\frac{(K_n-\mu)^2}{2\sigma^2}\right) \tag{37}$$

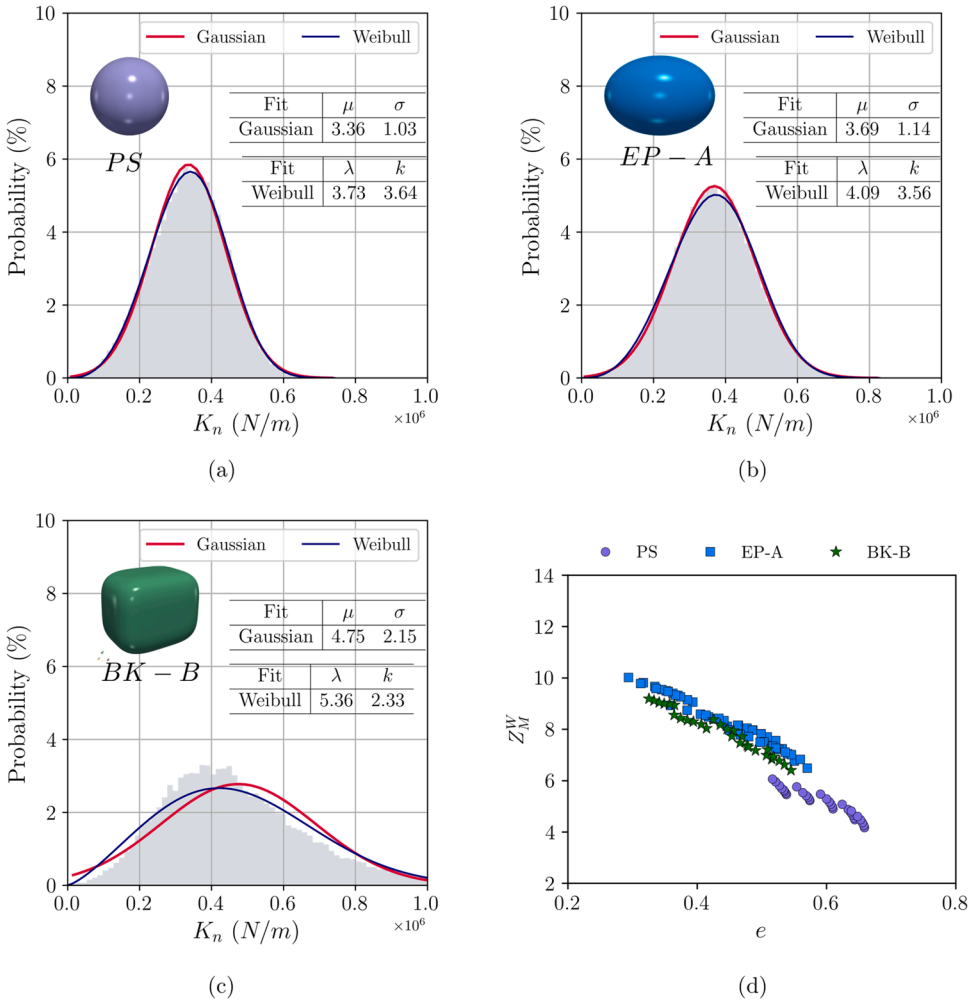

Fig. 17. (a)(b)(c) Illustrations of particle shape effect on the distribution of contact normal stiffness in packings with void ratio 0.552 under 50 kPa isotropic confining stress; (d) the relationship between the contact normal force weighted coordination number and void ratio, Z_M^W vs e.

and

$$w(K_n,\lambda,\kappa)=\frac{\kappa}{\lambda}\left(\frac{K_n}{\lambda}\right)^{k-1}\exp\left(-\left(\frac{K_n}{\lambda}\right)^{\kappa}\right) \tag{38}$$

where μ, σ, λ and κ are fitting parameters. For Gaussian distribution, both μ and σ increase as the particle shape changes from purely spherical to quasi-cuboid, indicating that both the mean contact normal stiffness and the uniformity increase. The Weibull distribution gives similar results that λ increases but κ decreases. As seen from Fig. 17, the Gaussian function gives slightly higher probability prediction of mean contact normal stiffness than Weibull function. Both two methods are found to be sufficient for describing the configurations of PS and EP-A specimens. With reference to the case BK-B, Weibull function seems to be more precise than the Gaussian function, where the broad range and zero values are considered.

To account for the observed differences brought by shape variation, we choose to apply a factor $\langle f_n/\langle f_n\rangle\rangle^{1/3}$ to each contact for calculating the contact numbers, where $\langle f_n\rangle$ denotes the averaged contact normal force. As plotted in Fig. 17d, the weighted coordination numbers, namely Z_M^W, are comparatively lower than the mechanical coordination number (see Fig. 16b). Together with the analysis on elastic wave velocities and contact network, it can be concluded that the elastic wave velocity is mainly dominated by the shape change of spherical to non-spherical, and the further alteration of blockiness will bring in opposite effect due to lower contact number and higher degree of non-homogeneity in spatial distribution of contact stiffness.

5. Conclusions

This study is aimed at addressing the fundamental question on the role of particle shape in wave propagation in granular media. A novel grain-scale model has been developed, which can cope with a huge number of non-spherical particles randomly packed to propagate elastic waves generated by very small perturbations, and efficient algorithms have been implemented to tackle the critical issues related to accurate detection of non-spherical particle contacts, boundary reflections and refractions, and elastic wave agitation. Both compression (P) and shear (S) waves are examined, and their characteristics are examined in time as well as frequency domain. The main results and observations are summarized as follows.

(1) The numerical model has exhibited an attractive capability in producing high-quality wave signals thus ensuring consistent wave velocities derived from both time and frequency domains. It successfully removes the ambiguities and uncertainties in physical and numerical experiments reported in the literature by using efficient techniques to treat sample dimensions, boundary conditions, transducers, and the calm-down process.
(2) A notable rise in elastic wave velocities takes place when the particle shape turns from spherical to ellipsoidal, confirming the experimental finding of Liu and Yang (2018); as the aspect ratio further increases (from 1.375 for EP-A to 1.625 for EP-B), the elastic wave velocity keeps increasing but within a rather limited range. Under otherwise similar conditions, higher frequency contents are preserved for ellipsoidal particle packings, whereas more prominent frequency filtering occurs in spherical particle packings.
(3) When particle shape evolves from pure ellipsoid towards quasi-cuboid, only a slight reduction in elastic wave velocities takes place. The characteristics of the dispersion relations are also similar except for reduced intensity of the peak branches for increased blockiness. In this regard, the blockiness effect is relatively minor when compared with the effect of particle aspect ratio.
(4) Packings of non-spherical particles in general have a broader range of void ratio and larger coordination numbers than packings of spherical particles. Specifically, particle elongation leads to substantial increase in packing density, connectivity and propagation speed. An additional increase of particle blockiness however reduces the coordination number as well as the uniformity of contact stiffness distribution.

Declaration of Competing Interest

The authors declare no conflict of interest.

Acknowledgment

The work was supported by the Research Grant Council (RGC) of Hong Kong under Nos. 17205717 and 17206418. The computations were performed using research computing facilities offered by the Information Technology Service (ITS) of The University of Hong Kong (HKU).

References

Anand, L., Gu, C., 2000. Granular materials: constitutive equations and strain localization. J. Mech. Phys. Solids 48, 1701–1733. https://doi.org/10.1016/S0022-5096(99)00066-6.
Andreotti, B., Forterre, Y., Pouliquen, O., 2013. Granular media: between fluid and solid. Cambridge University Press.
Bagi, K., 1996. Stress and strain in granular assemblies. Mech. Mater. 22, 165–177. https://doi.org/10.1016/0167-6636(95)00044-5.
Barr, A.H., 1981. Superquadrics and Angle-Preserving Transformations. IEEE Comput. Graph. Appl. 1, 11–23. https://doi.org/10.1109/MCG.1981.1673799.

Brunet, T., Jia, X., Mills, P., 2008. Mechanisms for acoustic absorption in dry and weakly wet granular media. Phys. Rev. Lett. 101, 2–5. https://doi.org/10.1103/PhysRevLett.101.138001.
Chang, C.S., Chao, S.J., Chang, Y., 1995. Estimates of elastic moduli for granular material with anisotropic random packing structure. Int. J. Solids Struct. 32, 1989–2008. https://doi.org/10.1016/0020-7683(94)00225-L.
Cheng, H., Luding, S., Saitoh, K., Magnanimo, V., 2020. Elastic wave propagation in dry granular media: Effects of probing characteristics and stress history. Int. J. Solids Struct. 187, 85–99. https://doi.org/10.1016/j.ijsolstr.2019.03.030.
Cho, G.-C., Dodds, J., Santamarina, J.C., 2006. Particle shape effects on packing density, stiffness, and strength: natural and crushed sands. J. Geotech. Geoenvironmental Eng. 132, 591–602. https://doi.org/10.1061/(ASCE)1090-0241(2006)132:5(591).
Christoffersen, J., Mehrabadi, M.M., Nemat-Nasser, S., 1981. A micromechanical description of granular material behavior. J. Appl. Mech. 48, 339–344. https://doi.org/10.1115/1.3157619.
Cundall, P.A., Strack, O.D.L., 1979. A discrete numerical model for granular assemblies. Géotechnique 29, 47–65. https://doi.org/10.1680/geot.1979.29.1.47.
De Graaf, J., Van Roij, R., Dijkstra, M., 2011. Dense regular packings of irregular nonconvex particles. Phys. Rev. Lett. 107, 1–5. https://doi.org/10.1103/PhysRevLett.107.155501.
Duffy, J., Mindlin, R.D., 1957. Stress-strain relation and vibrations of a granular medium. J. Appl. Mech., ASME 24, 585–593.
Gilles, B., Coste, C., 2003. Low-frequency behavior of beads constrained on a lattice. Phys. Rev. Lett. 90, 4. https://doi.org/10.1103/PhysRevLett.90.174302.
Goddard, J.D., 2014. Continuum modeling of granular media. Appl. Mech. Rev. 66 https://doi.org/10.1115/1.4026242.
Goddard, J.D., 1990. Nonlinear elasticity and pressure-dependent wave speeds in granular media. Proc. R. Soc. London. Ser. A Math. Phys. Sci. 430, 105–131. https://doi.org/10.1098/rspa.1990.0083.
Gu, X., Yang, J., Huang, M., 2013. Laboratory measurements of small strain properties of dry sands by bender element. Soils Found 53, 735–745. https://doi.org/10.1016/j.sandf.2013.08.011.
Gu, X.Q., Yang, J., 2013. A discrete element analysis of elastic properties of granular materials. Granul. Matter 15, 139–147. https://doi.org/10.1007/s10035-013-0390-3.
Hardin, B.O., Richart Jr, F.E., 1963. Elastic wave velocities in granular soils. J. Soil Mech. Found. Div. 89, 33–65.
Jaeger, H.M., Nagel, S.R., Behringer, R.P., 1996. Granular solids, liquids, and gases. Rev. Mod. Phys. 68, 1259–1273. https://doi.org/10.1103/RevModPhys.68.1259.
Jia, X., 2004. Codalike multiple scattering of elastic waves in dense granular media. Phys. Rev. Lett. 93, 8–11. https://doi.org/10.1103/PhysRevLett.93.154303.
Jia, X., Caroli, C., Velicky, B., 1999. Ultrasound propagation in externally stressed granular media. Phys. Rev. Lett. 82, 1863–1866. https://doi.org/10.1103/PhysRevLett.82.1863.
Johnson, K.L., 1985. Contact Mechanics. Cambridge University Press. https://doi.org/10.1017/CBO9781139171731.
Kawamoto, R., Andò, E., Viggiani, G., Andrade, J.E., 2018. All you need is shape: Predicting shear banding in sand with LS-DEM. J. Mech. Phys. Solids 111, 375–392. https://doi.org/10.1016/j.jmps.2017.10.003.
Kildashti, K., Dong, K., Samali, B., 2018. A revisit of common normal method for discrete modelling of non-spherical particles. Powder Technol 326, 1–6. https://doi.org/10.1016/j.powtec.2017.11.066.
Leonard, A., Ponson, L., Daraio, C., 2014. Wave mitigation in ordered networks of granular chains. J. Mech. Phys. Solids 73, 103–117. https://doi.org/10.1016/j.jmps.2014.08.004.
Lin, X., Ng, T.-T., 1995. Contact detection algorithms for three-dimensional ellipsoids in discrete element modelling. Int. J. Numer. Anal. Methods Geomech. 19, 653–659. https://doi.org/10.1002/nag.1610190905.
Liu, X., Yang, J., 2018. Shear wave velocity in sand: effect of grain shape. Géotechnique 68, 742–748. https://doi.org/10.1680/jgeot.17.T.011.
Lu, G., Third, J.R., Müller, C.R., 2015. Discrete element models for non-spherical particle systems: From theoretical developments to applications. Chem. Eng. Sci. 127, 425–465. https://doi.org/10.1016/j.ces.2014.11.050.
McDowell, G.R., Bolton, M.D., Robertson, D., 1996. The fractal crushing of granular materials. J. Mech. Phys. Solids 44, 2079–2101. https://doi.org/10.1016/S0022-5096(96)00058-0.
Mindlin, R.D., 1949. Compliance of elastic bodies in contact. J. Appl. Mech., ASME 16, 259–268.
Mouraille, O., Luding, S., 2008. Sound wave propagation in weakly polydisperse granular materials. Ultrasonics 48, 498–505. https://doi.org/10.1016/j.ultras.2008.03.009.
Nedderman, R.M., 1992. Statics and kinematics of granular materials. Cambridge University Press, Cambridge. https://doi.org/10.1017/CBO9780511600043.
Nixon, S.A., Chandler, H.W., 1999. On the elasticity and plasticity of dilatant granular materials. J. Mech. Phys. Solids 47, 1397–1408. https://doi.org/10.1016/S0022-5096(98)00108-2.
O'Donovan, J., O'Sullivan, C., Marketos, G., Muir Wood, D., 2015. Analysis of bender element test interpretation using the discrete element method. Granul. Matter 17, 197–216. https://doi.org/10.1007/s10035-015-0552-6.
Oda, M., 1982. Fabric tensor for discontinuous geological materials. Soils Found 22, 96–108. https://doi.org/10.3208/sandf1972.22.4_96.
Patel, A., Bartake, P., Singh, D., 2009. An empirical relationship for determining shear wave belocity in granular materials accounting for grain morphology. Geotech. Test. J. 32, 1–10. https://doi.org/10.1520/GTJ100796.
Podlozhnyuk, A., Pirker, S., Kloss, C., 2017. Efficient implementation of superquadric particles in Discrete Element Method within an open-source framework. Comput. Part. Mech. 4, 101–118. https://doi.org/10.1007/s40571-016-0131-6.
Rothenburg, L., Kruyt, N.P., 2004. Critical state and evolution of coordination number in simulated granular materials. Int. J. Solids Struct. 41, 5763–5774. https://doi.org/10.1016/j.ijsolstr.2004.06.001.
Roux, J.N., 1997. Contact disorder and non-linear elasticity of granular packings: a simple model. Powder and Grains 97, 215–218.
Rudnicki, J.W., Rice, J.R., 1975. Conditions for the localization of deformation in pressure-sensitive dilatant materials. J. Mech. Phys. Solids 23, 371–394. https://doi.org/10.1016/0022-5096(75)90001-0.
Saitoh, K., Shrivastava, R.K., Luding, S., 2019. Rotational sound in disordered granular materials. Phys. Rev. E 99, 1–12. https://doi.org/10.1103/PhysRevE.99.012906.
Santamarina, J.C., Klein, K.A., Fam, M.A., 2001. Soils and Waves: Particulate Materials Behavior, Characterization and Process Monitoring, Lasers and Fibre Optics Series. Wiley.
Satake, M., 1976. Constitution of mechanics of granular materials through graph representation. Theor. Appl. Mech. 26, 257–266.
Satake, M., Jenkins, J.T., 1988. Micromechanics of Granular Materials, ISSN. Elsevier Science.
Sharifipour, M., Dano, C., Hicher, P.-Y., 2004. Wave velocities in assemblies of glass beads using bender-extender elements. In: 17th ASCE Engineering Mechanics Conference.
Soltanbeigi, B., Podlozhnyuk, A., Papanicolopulos, S.A., Kloss, C., Pirker, S., Ooi, J.Y., 2018. DEM study of mechanical characteristics of multi-spherical and superquadric particles at micro and macro scales. Powder Technol 329, 288–303. https://doi.org/10.1016/j.powtec.2018.01.082.
Somfai, E., Roux, J.N., Snoeijer, J.H., Van Hecke, M., Van Saarloos, W., 2005. Elastic wave propagation in confined granular systems. Phys. Rev. E 72, 1–18. https://doi.org/10.1103/PhysRevE.72.021301.
Spencer, A.J.M., 1964. A theory of the kinematics of ideal soils under plane strain conditions. J. Mech. Phys. Solids 12, 337–351. https://doi.org/10.1016/0022-5096(64)90029-8.
Tang, X., Yang, J., 2018. Modelling wave propagation in dry granular materials. In: Giovine, P., Mariano, P.M., Mortara, G. (Eds.), Micro to MACRO Mathematical Modelling in Soil Mechanics. Springer International Publishing, Cham, pp. 373–381.
Terzopoulos, D., Metaxas, D., 1991. Dynamic 3D models with local and global deformation: deformable superquadrics. IEEE Trans. Pattern Anal. Mach. Intell. 13, 703–714.
Thornton, C., 2000. Numerical simulations of deviatoric shear deformation of granular media. Géotechnique 50, 43–53. https://doi.org/10.1680/geot.2000.50.1.43.
Vergara, L., 2010. Model for dissipative highly nonlinear waves in dry granular systems. Phys. Rev. Lett. 104, 1–4. https://doi.org/10.1103/PhysRevLett.104.118001.

Walton, K., 1987. The effective elastic moduli of a random packing of spheres. J. Mech. Phys. Solids 35, 213–226. https://doi.org/10.1016/0022-5096(87)90036-6.
Waymel, R.F., Wang, E., Awasthi, A., Geubelle, P.H., Lambros, J., 2018. Propagation and dissipation of elasto-plastic stress waves in two dimensional ordered granular media. J. Mech. Phys. Solids 120, 117–131. https://doi.org/10.1016/j.jmps.2017.11.007.
Wei, L.M., Yang, J., 2014. On the role of grain shape in static liquefaction of sand–fines mixtures. Géotechnique 64, 740–745. https://doi.org/10.1680/geot.14.T.013.
Wellmann, C., Lillie, C., Wriggers, P., 2008. A contact detection algorithm for superellipsoids based on the common-normal concept. Eng. Comput. 25, 432–442. https://doi.org/10.1108/02644400810881374.
Yamashita, S., Kawaguchi, T., Nakata, Y., Mikami, T., Fujiwara, T., 2009. Interpretation of international parallel test on the measurement of Gmax using bender elements. Soils Found. Shibuya, S., 49, 631–650. https://doi.org/10.3208/sandf.49.631.
Yang, J., Gu, X.Q., 2013. Shear stiffness of granular material at small strains: does it depend on grain size? Géotechnique 63, 165–179. https://doi.org/10.1680/geot.11.P.083.
Yang, J., Luo, X.D., 2015. Exploring the relationship between critical state and particle shape for granular materials. J. Mech. Phys. Solids 84, 196–213. https://doi.org/10.1016/j.jmps.2015.08.001.
Yang, J., Wei, L.M., 2012. Collapse of loose sand with the addition of fines: The role of particle shape. Géotechnique 62, 1111–1125. https://doi.org/10.1680/geot.11.P.062.
Yuan, Y., Liu, L., Zhuang, Y., Jin, W., Li, S., 2018. Coupling effects of particle size and shape on improving the density of disordered polydisperse packings. Phys. Rev. E 98, 42903. https://doi.org/10.1103/PhysRevE.98.042903.
Zhao, S., Evans, T.M., Zhou, X., 2018. Effects of curvature-related DEM contact model on the macro- and micro-mechanical behaviours of granular soils. Géotechnique 68, 1085–1098. https://doi.org/10.1680/jgeot.17.P.158.